

# Modeling texture and microstructural evolution in the equal channel angular extrusion process

I.J. Beyerlein\*, R.A. Lebensohn, C.N. Tomé

*Los Alamos National Laboratory, Los Alamos, NM 87545, USA*

Received 24 March 2002; received in revised form 6 June 2002

## Abstract

In this work, we develop a modeling framework for predicting the visco-plastic deformation, microstructural evolution (distributions of grain shape and size) and texture evolution in polycrystalline materials during the equal channel angular extrusion (ECAE) process, a discontinuous process of severe shear straining. The foundation of this framework is a visco-plastic self-consistent (VPSC) scheme. We consider a  $90^\circ$  die angle and simulate ECAE up to four passes for four processing routes, (A, C,  $B_A$  and  $B_C$ , as denoted in the literature) for an FCC polycrystalline material. We assume that the FCC single crystal has a constant critical resolved shear stress (CRSS), so that hardening by dislocation activity is suppressed, and the influence of grain shape distribution and texture as well as their interaction can be isolated. Many deformation microstructural features, such as grain size and shape distribution, texture, and geometric hardening–softening, were highly dependent on processing route. Using a grain subdivision criterion based on grain shape, route A was the most effective, then route  $B_A$  and route  $B_C$  and lastly route C, the least effective for grain size refinement, in agreement with redundant strain theory. For producing refined equiaxed grains, route  $B_C$  was more effective than routes  $B_A$  and A. We show that grain–grain interactions tend to weaken texture evolution and consequently geometric hardening and softening in all routes.

© 2002 Elsevier Science B.V. All rights reserved.

*Keywords:* Severe plastic deformation; Strain path changes; Visco-plasticity; Grain size and shape distributions; Grain–grain interactions; Grain refinement

## 1. Introduction

Equal channel angular extrusion (ECAE) [1] is so far the only technique that can produce ultrafine-grained materials large enough for structural components. Polycrystalline materials processed by ECAE have a unique microstructure [1–10] and remarkable mechanical properties: ultra-high strength and high ductility [1,2,5,10], as well as superplastic forming behavior [1,2]. The concomitant high strength and ductility observed in ECAE materials challenge our current understanding of microstructure–property relationships of metals processed by severe plastic deformation. Development of a large strain deformation polycrystalline constitutive law will be a necessary tool for predicting the final deforma-

tion microstructures and possibly modifying the process for an optimum combination of material properties.

The ECAE process imposes multiple changes in strain path and large strain deformation on the sample. ECAE is a discontinuous process, involving inserting and re-inserting the sample in a die (see Fig. 1a), which contains two channels with equal cross-section, intersecting at an angle  $\Phi$  [1]. As it is forced to pass through the die, the sample is severely deformed in shear as it changes its direction by the die angle  $\Phi$ , typically ranging from as low as  $90^\circ$  to as high as  $157.5^\circ$  [1,10]. The sample undergoes no change in shape so the ECAE processing route can involve any number of passes through the die. As reported in the current literature (see [4] for review), the number of passes used has ranged from one to 16, utilizing one of four popular ECAE routes, labeled A, C,  $B_A$  and  $B_C$  [4,6,8]. The routes are distinguished by either clockwise (CW) or counterclockwise (CCW) rotations, usually about the sample's bar axis (see Fig.

\* Corresponding author

E-mail address: irene@lanl.gov (I.J. Beyerlein).

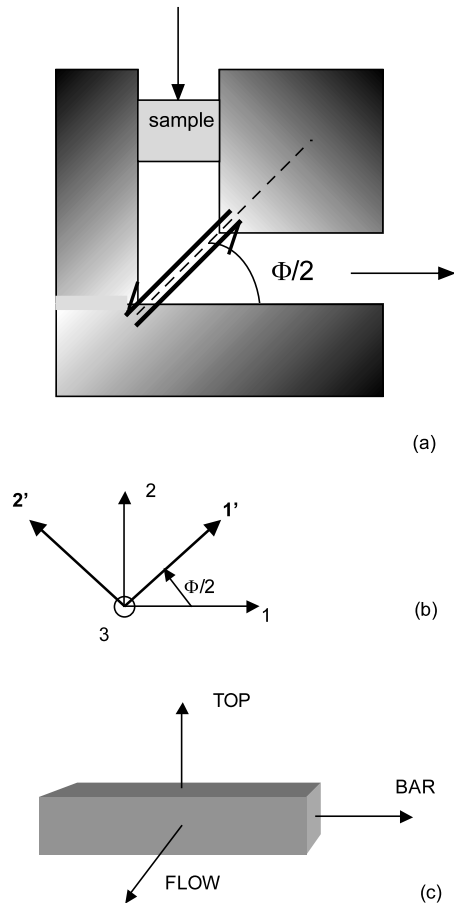


Fig. 1. (a) Schematic of the ECAE process with  $\Phi/2 = 45^\circ$  die angle and (b) global coordinate system (1, 2, 3) considered in the model and the shear plane coordinate system, (1', 2', 3). (c) Schematic of the coordinate system centered in the sample after it exits an ECAE pass.

1b), between subsequent ECAE passes: A, no bar axis rotation; C,  $180^\circ$  rotation after every pass;  $B_A$ , CW  $90^\circ$  rotation after even numbered passes and CCW  $90^\circ$  after odd numbered passes; and  $B_C$ , CW  $90^\circ$  rotation after every pass. All possible ECAE routes lead to changes in strain path, including the original route A that involves no intermediate rotation about the sample bar axis between passes.

The unique microstructure developed after several passes is responsible for the extraordinary properties of ECAE materials [1,2]. To date there are many experimental studies that demonstrate that ECAE can potentially refine the grain size of coarse-grained pure metals and alloys to at least a few hundred nanometers,  $\sim 0.2\text{--}0.4\ \mu\text{m}$  [1–3,5,7–10] and produce an equiaxed microstructure. It is not rare for the grains to refine significantly within the first pass and achieve equiaxed, submicron average grain (and/or subgrain) sizes by the end of 4–16 passes with high angle grain boundaries [1,2,5,7–10]. However, the processing parameters recommended for rapid grain refinement differ from study to study.

This is not surprising considering the complex nature of the process and indeed there are several factors to consider. Firstly, it is likely that the best processing route depends on the material, (e.g. crystal structure, stacking fault energy, alloying elements [3,4]) and on processing mechanics and parameters, such as die angle  $\Phi$ , temperature, applied pressure, lubrication, and die design [3,10]. For instance, for pure Al and  $\Phi = 90^\circ$ , route  $B_C$  is found to be more effective than  $B_A$  for grain refinement [6,8], whereas for an Al alloy and  $\Phi = 120^\circ$ , the opposite is true [9]. Secondly, the microstructures created by ECAE are rather unique, complex, and inhomogeneous and can therefore be challenging to characterize, particularly in 3D. The grain sizes and shapes are statistical in nature and their distributions have proven to be sensitive to the processing route [5,7–10]. ECAE microstructures typically consist of a mix of low and high angle grain boundaries varying widely in structure [2] and leaves one to distinguish between grains and subgrains and between subgrains and cellular structures. Thirdly the interaction between texture and microstructure evolution is strong and so it is possible that the initial sample texture can influence the resulting degree of grain refinement. Thus the initial textures used across the ECAE studies mentioned above may not have been the same. Lastly, one finds that the definition of ‘success’ or ‘effectiveness’ in grain refinement can refer to either nanosized dimensions or equiaxed shapes or both.

The final desired microstructures (distribution of grain size, shape and crystallographic orientation) depend on the desired properties. Thus one needs a reliable predictive method to relate microstructure to material properties. Once we understand why one route is better than the other in this respect, then we can reliably design this process for many suitable materials and applications.

To this end, modeling texture<sup>1</sup> evolution is an important first step. In large strain deformation of a polycrystal, strong texture can develop and greatly influence the flow response [11]. The texture developed will determine the anisotropic response of the ECAE material under subsequent deformation, as well as some physical properties (e.g. magnetic) [1]. Texture development may also play a role in the grain refinement of the ECAE polycrystalline material since the intragranular microstructure developed may vary from grain to grain and depend on individual grain orientation with respect to the loading axis. Thus grain orientation will determine the subgrain microstructure and in turn, the

<sup>1</sup> Texture is a term that describes the distribution of crystallographic orientations in a polycrystalline material. Here crystallographic orientation of the grain is given with respect to global axes in Fig. 1b.

subgrain microstructure will govern the subdivision process and grain–subgrain orientations.

The impact is especially great in the ECAE process, since changes in strain path occur with each pass. In each pass, orientations of material texture and grain morphology with respect to the shear plane are altered and such changes will influence the propensity of grains to plastically co-deform, subdivide, or slide relative to one another.

To date the relationships between texture development, ECAE route, and grain refinement during the ECAE process have not been systematically studied theoretically [4]. Particularly in these situations of large strain and strain path changes, the coupling between texture, grain size, and subgrain dislocation structures is usually strong and cannot be neglected. No single model to date is capable of simulating the ensemble of mechanisms responsible for grain refinement under these situations. So not all of these factors will be addressed here. Rather in this work the focus is modeling plastic deformation under severe plastic strains and strain path changes accounting for texture and grain shape evolution alone. We do so at the expense of making some simplifying assumptions on admittedly some important features. First we intentionally suppress the influences of dislocation activity (forest hardening and grain size dependence) by imposing a constant critical resolved shear stress (CRSS) for the single crystals in the aggregate. Second we employ an empirical grain subdivision law to predict the evolution of the statistical distributions of grain shape and size. To reveal the effects of the various changes in strain path, we compare the same outcomes under monotonic shear straining. The influence of grain–grain interactions is also examined. Upcoming modeling efforts that couple microstructural features, such as deformation grain morphology, texture, and evolving sub-grain structures, will use the modeling framework introduced here.

## 2. Constitutive modeling of ECAE

### 2.1. Visco-plastic self-consistent model

Modeling texture, microstructural evolution, and macroscopic polycrystalline response is accomplished here using the visco-plastic self-consistent (VPSC) polycrystal model [12,13]. We prefer to build our ECAE simulation using this polycrystalline model for several reasons. The polycrystalline aggregate is represented by several hundred grains, each with a distinct orientation and volume fraction. The VPSC model treats each grain as an ellipsoidal visco-plastic inclusion interacting with the effective medium represented by the average response of all the grains. This treatment of each grain allows local equilibrium and compatibility to be satis-

fied, while maintaining computational efficiency. The assumption of visco-plasticity neglects elastic effects and appropriately applies to processes involving large plastic deformation, such as ECAE. VPSC also accounts for the plastic anisotropy of each grain; each grain is allowed to deform differently depending on its morphological<sup>2</sup> and crystallographic orientations with respect to the surrounding homogeneous effective medium. This feature will be particularly important when considering crystal symmetries other than cubic, such as HCP Mg, Be and Ti. As a result the model provides the number of active slip modes in each grain, and grain rotation and distortion with each increment in strain. This local calculation leads to a prediction of statistical dispersion in these values. Such local information also is necessary for incorporating grain–grain interaction, substructure evolution and grain refinement models, some of which we introduce here in simple form. Interaction between grain and macroscopic polycrystalline response is accounted for since the individual responses of all the grains (visco-plastic modulus and stress partitioning) are averaged to calculate the modulus of the effective medium.

Agnew et al. [14] compared measured (111) pole figures with those predicted with VPSC (without grain refinement or grain–grain interactions unlike in this work) and a Taylor model<sup>3</sup> for ECAE copper, and showed that VPSC textures agree better with experimental texture data. The Taylor model textures were sharper than either the data or VPSC textures and it did not capture some features observed in the third and fourth ECAE passes. Reasons for this were attributed to the difference in the number of active slip systems predicted by the models.

General input into our model are the initial grain orientation and shape distribution and constitutive response of the grains. For this work, the model material is single phase with a FCC crystal structure. The initial polycrystal is non-textured, consisting of 500 spherical grains with randomly generated discrete orientations, each with equal volume fraction. We also assume that the CRSS in the single crystal is constant, without hardening. With this simplistic constitutive relation we can isolate the geometric effects associated with texture evolution from the single crystal hardening associated with dislocation evolution and grain size effects. Strain hardening can mask the effect of geometric softening–hardening, though the connection with experimental results will be stronger. Once the geometric effects are understood, we will predict deformation

<sup>2</sup> Morphological orientation is the orientation of the three axes of the ellipsoidal grain.

<sup>3</sup> See [13] for review of polycrystalline models such as the Taylor model.

microstructures resulting from a more realistic single crystal constitutive law, such as one based on the mechanical threshold stress theory [15] or on strain gradient theories [16–18], which take into account hardening due to increasing dislocation density or decreasing grain size.

## 2.2. ECAE shear strains and rotations

The ECAE route is a discontinuous process that imposes high shear strains and sequential changes in strain path on the sample. In each ECAE pass we assume simple shear occurs uniformly in the sample<sup>4</sup>. The magnitude of simple shear  $\gamma$  along the shear plane, parallel to  $\Phi/2$ , has been estimated to be [19]:

$$\gamma = 2 \cot\left(\frac{\Phi}{2}\right) \quad (1)$$

For this work, we consider only the case in which the die angle is  $90^\circ$ , as illustrated in Fig. 1a, and thus Eq. (1) results in  $\gamma = 2$  (or shear strain  $\varepsilon_{12} = 1$ ) along the  $45^\circ$  slip plane for every pass. In a coordinate system parallel to the slip plane,  $1'-2'$ , (see Fig. 1b), the applied velocity gradient tensor is:

$$\dot{L} = \begin{pmatrix} 0 & -\dot{\gamma} & 0 \\ 0 & 0 & 0 \\ 0 & 0 & 0 \end{pmatrix} \quad (2)$$

where  $\dot{\gamma}$  is the constant applied rate. We choose a time increment  $\Delta t$  and impose  $\Delta\gamma$  such that  $\Delta\gamma = \dot{\gamma}\Delta t$ . In simulating ECAE, we find it advantageous to express Eq. (2) in the global coordinate system, illustrated in Fig. 1b, as 1-axis, 2-axis and 3-axis, that remains fixed during the ECAE process. In the global coordinate system, Eq. (2) becomes:

$$\dot{L} = \begin{pmatrix} \cos\theta \sin\theta \dot{\gamma} & -\cos^2\theta \dot{\gamma} & 0 \\ \sin^2\theta \dot{\gamma} & -\cos\theta \sin\theta \dot{\gamma} & 0 \\ 0 & 0 & 0 \end{pmatrix} \quad (3)$$

where  $\theta = (90^\circ - \Phi/2)$ .

We can now proceed to modeling the four common ECAE processing routes A, C, B<sub>A</sub> and B<sub>C</sub>. To simulate the associated sample rotation schemes, we rotate rigidly the crystallographic texture and the morphology of the grains after each pass relative to the global coordinate system. One advantage in performing these rotations and deformations relative to the global coordinates is that the location of the shear plane does not change

during the ECAE process, and the velocity gradient Eq. (3) always has the same form. However, with each ECAE pass the orientation of the sample texture will change relative to the global coordinate system as the sample passes through the die and experiences the associated ECAE route rigid rotations.

To begin, let us consider the axes of the sample as it exits the die, labeled as bar, top and flow (Fig. 1c). For our  $90^\circ$  die, the sample exits the die with the bar axis oriented along 1-axis, the top axis along 2-axis, and the flow axis along 3-axis. After each pass, the sample experiences one or two rigid body rotations depending on the ECAE route. First in every case, the morphological and crystallographic textures are rotated CW  $(180^\circ - \Phi) = 90^\circ$  about the 3-axis (from the horizontal to the vertical position) to simulate the re-insertion of the 'head' of the sample into the die entrance. This first rotation orients the sample such that the bar, top, and flow axes are aligned with the  $-(2\text{-axis})$ , 1-axis, and 3-axis of the global coordinate system, respectively.

The second rotation about the global 2-axis (now sample bar axis) depends on the route and pass number. For route A, the textures are not rotated a second time. For route C, the textures are rotated  $180^\circ$  after every pass. For route B<sub>A</sub>, the textures are rotated CW  $90^\circ$  after each odd pass and CCW  $90^\circ$  after each even pass. For route B<sub>C</sub>, the textures are rotated CW  $90^\circ$  after every pass. Note that the first pass is the same for all four routes and that the first and second passes are the same for routes B<sub>A</sub> and B<sub>C</sub>.

All four ECAE routes lead to changes in the shear strain path. In routes A, B<sub>A</sub> and B<sub>C</sub>, the shear planes intersect between sequential passes, resulting in a cross-shear strain path. In contrast, the strain path of route C is shear reversal. In the second pass of route C, the texture experiences a reverse shear along the  $\Phi/2$  direction and a forward shear in the third pass and so on. In route B<sub>C</sub>, there is shear reversal, though it is not sequential; the third pass is the reverse shear of the first pass and the fourth pass is the reverse shear of the second pass [4,6]. The strain path patterns of all four routes repeat every four passes.

In the simulation, the ECAE route can involve any number of passes  $N$  to impose a higher strain,  $\gamma_N = N\gamma$ , Eq. (1). It is not uncommon for the ECAE procedure to involve from 10 to 16 passes to produce the desired, equiaxed, submicron grain structure having primarily high angle grain boundaries [1,2,4].

## 2.3. Grain subdivision rule

The process of grain refinement is qualitatively summarized as follows. Under large strain deformations the dislocation walls that later form subgrains or cell blocks with low angle grain boundaries develop within the grains. The characteristics and orientation of these

<sup>4</sup> This assumption is valid for a polycrystalline element within the shear zone and in the center of the sample. Realistically, the strain distribution varies across the sample section as well as along the sample axis, as a result of, for instance, frictional effects at the die/sample interface. To simulate this effect, our VPSC based constitutive model can be incorporated into a finite element simulation code, for instance, to account for these inhomogeneous strain fields [20].

dislocation walls depend on the orientation of the grain with respect to loading [11,21–23]. With more passes, rotation of these subgrains under deformation leads to higher angle boundaries between subgrains. Typically when the misorientation angle is high enough (e.g.  $> 15^\circ$ ), subgrains are then considered to be grains. Studies show that in most cases grain refinement is significant during the first two passes and saturates with additional passes [5,7], while ECAE passes beyond the first four-pass cycle serve to increase the misorientation between the subgrain structures. Very little of the original grain boundaries remains after several passes [24].

In the model under shear deformation, grains of different orientations evolve into variously shaped ellipsoids, leading to a dispersion in grain shape. The grain shape evolution of individual grains predicted by VPSC mimics the process that takes place in the real aggregate up to low values of grain aspect ratio, since each grain is assumed to have a homogeneous stress state. When the grains become severely distorted they will not maintain relatively uniform internal stress states as assumed by the VPSC model. Rather, realistically, through the formation of cell walls and the local interactions with neighbors, they partition into subgrains.

In light of general experimental observations of grain refinement and the assumptions of the VPSC model, we employ an empirical criterion for the grain subdivision process during ECAE. Our simple criterion partitions the grain into smaller grains, neglecting intermediate steps of subgrain development, and is based on grain shape, as illustrated in Fig. 2. In the model, grain shape is described by three ellipsoid axes (given by the eigenvalues of the accumulated distortion tensor): the long, medium and short axes with lengths  $L$ ,  $M$  and  $S$ , respectively. The single subdivision (Fig. 2a) and double subdivision (Fig. 2b) criteria<sup>5</sup> are satisfied when the two ratios,  $L/S$  and  $M/S$ , achieve critical values,  $R$  and  $R/2$ , respectively, following:

$$\frac{L}{S} > R \quad \text{and} \quad \frac{M}{S} < \frac{R}{2}$$

(single subdivision criterion, Fig. 2a)

or

$$\frac{L}{S} > R \quad \text{and} \quad \frac{M}{S} > \frac{R}{2} \quad (4)$$

(double subdivision criterion, Fig. 2b)

According to these criteria, either the long axis or both the medium and long axes may divide in half. The first

criterion, where an elongated grain is divided into two smaller grains (Fig. 2a), is more characteristic of shear. The latter criterion, where a flat grain is divided into four smaller grains (Fig. 2b), is more characteristic of rolling or axisymmetric compression.

In the VPSC code, the evolution of the shape of each individual grain is accounted for in the calculation and is tracked throughout the process. In every deformation step, the criteria Eq. (4) are checked for each grain orientation and, when met, the grain shape is redefined accordingly, while the grain orientation and total volume fraction are not modified. If a given orientation of volume fraction  $V_f$  meets the first criterion, the long axis of the grain is divided into two equal size grains each with the same orientation as the parent and each with  $V_f/2$  (see Fig. 2a). If the second criterion is satisfied, then both the long and medium axes of the grain are divided into four equal size grains each with the same orientation as the parent and with volume fraction  $V_f/4$  (see Fig. 2b).

The subdivision criteria employed here are empirical and only consider the influence of shape, but not the intragranular microstructure. However, these criteria are based on previous rolling simulations employing an N-site VPSC scheme that predicts intragranular misorientations exceeding  $15^\circ$  for grain aspect ratios of about 5 [26]. In the calculations that follow we assume a fixed critical ratio  $R = 5$  in Eq. (4), but certainly there are

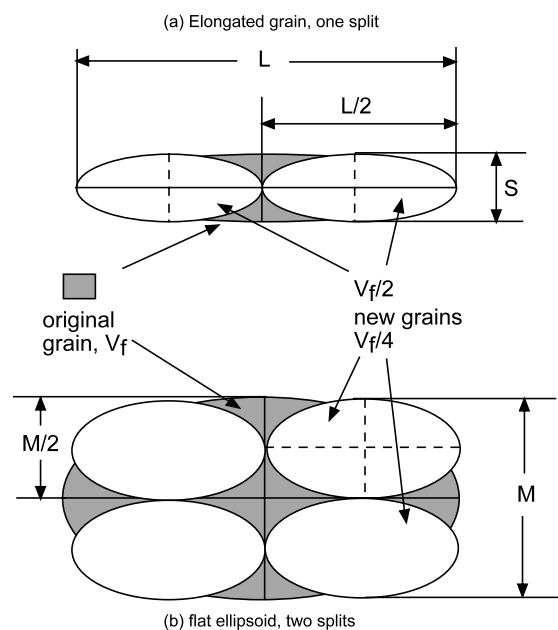


Fig. 2. Schematic illustrating the grain subdivision models used in the ECAE simulation: (a) single split of grain into two equal size grains and (b) double split of grain into four equal size grains. Either subdivision process occurs when the corresponding criterion in Eq. (4) is satisfied.

<sup>5</sup> We would like to note that these criteria are slightly different than those used in [25], wherein the medium and long axes were allowed to split independently.

other reasonable values of  $R$  dependent on material and not on loading conditions.

Without invoking some sort of subdivision scheme, the imposed strains in ECAE are so severe that the aspect ratios of the grains (i.e. long to short axes ratio) become unrealistically large, approximately 30–50 after four passes. Obviously different domains of heavily deformed grains will interact more strongly with neighboring grains and the concept of a monolithic orientation is somewhat lost. Certainly other mechanisms are involved in grain subdivision, but it is reasonable to expect that these grains will subdivide before they reach such extreme shapes.

#### 2.4. Grain co-rotation

In a recent paper [27] the effect of grain–grain interactions upon texture and anisotropy evolution is analyzed. In the present work, we implement a ‘grain co-rotation’ scheme in VPSC, where orientations are paired at random at the beginning of the simulation, and the paired ellipsoids are made to co-rotate, in order to enforce compatibility conditions at grain boundaries. We verified that this scheme leads to a slower texture evolution and provides better agreement with experimental ECAE textures [28]. The corresponding textures are qualitatively the same as those in Fig. 3 but scaled down in intensity. As a consequence, it will also affect the geometric hardening in the polycrystalline material associated with texture development and for this reason we will compare the evolution of yield stress predicted with and without the co-rotation assumption. Lastly, grain–grain interaction does not affect substantially the grain shape evolution and hence grain subdivision by Eq. (4).

### 3. Results

This section presents results on the evolution of yield stress, texture and grain size and shape using the VPSC code for an FCC single phase polycrystalline aggregate deforming by slip on the (111)[110] systems. The material is initially non-textured. The model material was subjected to four passes using the four standard ECAE processing routes, A, C, B<sub>A</sub> and B<sub>C</sub>. By the end of four passes, all four routes complete a cycle and return to the original shear direction and shear plane of the first pass. For the purpose of investigating the influence of processing route, applying our model for up to four passes is adequate. For every pass, the sample undergoes a uniform simple shear strain along the  $\Phi/2 = 45^\circ$  slip plane at a constant shear rate of  $0.01 \text{ s}^{-1}$ .

To illustrate the influence of strain path changes characteristic of all four ECAE routes, we apply our model to predict the grain refinement and textures under

monotonically increasing simple shear up to the same amount of total applied shear strain as each of the four  $\Phi = 90^\circ$  ECAE passes.

In the calculations that follow, we set  $R = 5$  in the subdivision criteria Eq. (4). This should reflect the fact that in a grain with a shape aspect ratio of 5, disjoint domains within the grain are likely to be independently influenced by their surroundings and become disconnected. Needless to say, the predicted rate of grain splitting will highly depend on the value of  $R$  employed, but the trends across routes, however, are unchanged.

#### 3.1. Deformation textures exiting each pass

In our model, the ECAE routes are defined by a series of shear passes and rigid sample rotations that result in changes in the relative orientation of the applied shear plane of the current pass with the texture resulting from the previous pass. First we investigate how such changes influence sample texture after each pass. Fig. 3 displays (111) pole figures represented in the 1–2 plane of the global coordinate system, after each pass and before the associated subsequent rotations. The textures up to four passes and for all four routes are displayed. The shear plane is  $45^\circ$  (CCW) from the 1-axis in all these pole figures as in Fig. 1a. The model material initially had random texture and by the end of the first pass we predict typical simple shear textures with maximum intensities of about 7 m.r.o.

In subsequent passes, the textures clearly are highly dependent on the processing route and number of passes. In the second to fourth passes, route A induces roughly identical textures after each pass, without a significant change in the intensity. Route C, on the other hand, reverses the shear direction after each pass and, as a consequence, tends to randomize the texture after the even passes. As a consequence, route C produces the weakest texture with maximum intensities of about 2 m.r.o. As for routes B<sub>A</sub> and B<sub>C</sub>, the  $90^\circ$  rotation after each pass introduces shear on a different plane. The final result is a rather ‘mixed’ type of texture with higher intensities after each subsequent pass than those generated in the texture for route A or C.

In general the peak intensities and location of the maximum depend on the processing route and pass. The maximum density (111) pole is closely aligned with the shear plane normal after passes 2 and 4 of route B<sub>C</sub>, passes 2 and 3 of route B<sub>A</sub>, and passes 2–4 of route A. The strongest texture after pass 3 and 4 corresponds to route B<sub>A</sub>.

Fig. 3 includes the (111) deformation texture after monotonic straining up to shear strains,  $\epsilon_{12} = 1.0, 2.0, 3.0$  and  $4.0$ , for two cases, with and without subdivision. As shown, the deformation texture with grain subdivision looks similar to the one of route A, having nearly the same intensities. The deformation texture for route

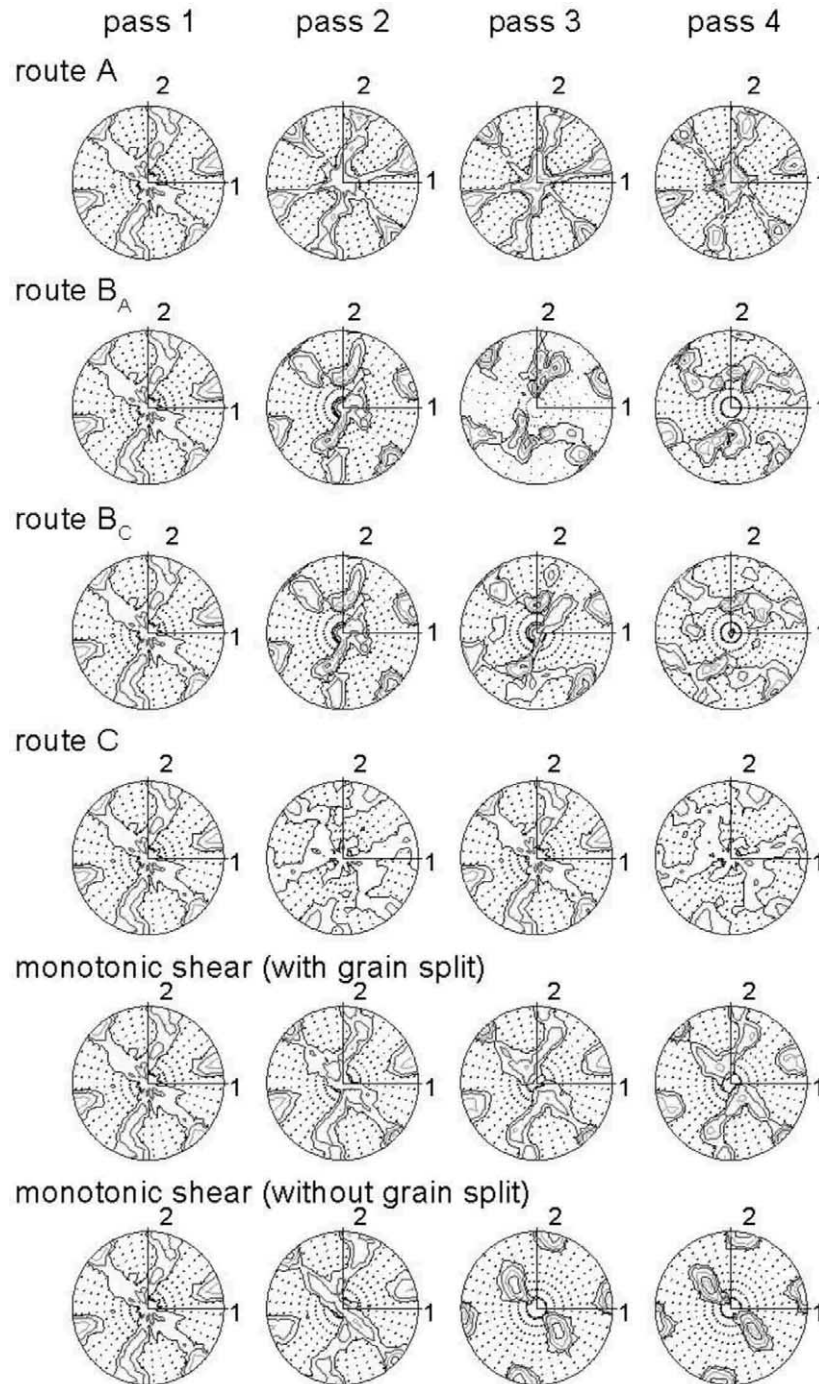


Fig. 3. (111) pole figures in sample exiting each pass up to four passes for the four ECAE routes. Also shown are the (111) pole figures for a monotonically shear strained sample (with and without grain subdivision) for accumulated strains equivalent to that accumulated in each pass. The intensity levels plotted correspond to 1, 2, 4, 7, 11, 16 multiple of random orientations. The shear plane and coordinate system used in these pole figures are shown in Fig. 1a.

A, however, appears to be slightly stronger with differences between these two cases growing with strain level. Though the shear planes between sequential passes intersect at  $90^\circ$ . Our results suggest that route A does provide more continuity in deformation textures than the other routes, particularly B<sub>A</sub> and B<sub>C</sub>.

Comparing the textures of the two monotonic strain-ing cases suggests that our shear textures are influenced by grain shape. Under large accumulated strains, i.e. after passes 3 and 4, the shapes of the grains become severely elongated with aspect ratios of  $\sim 30\text{--}50$  when grain subdivision is suppressed. As expected, when

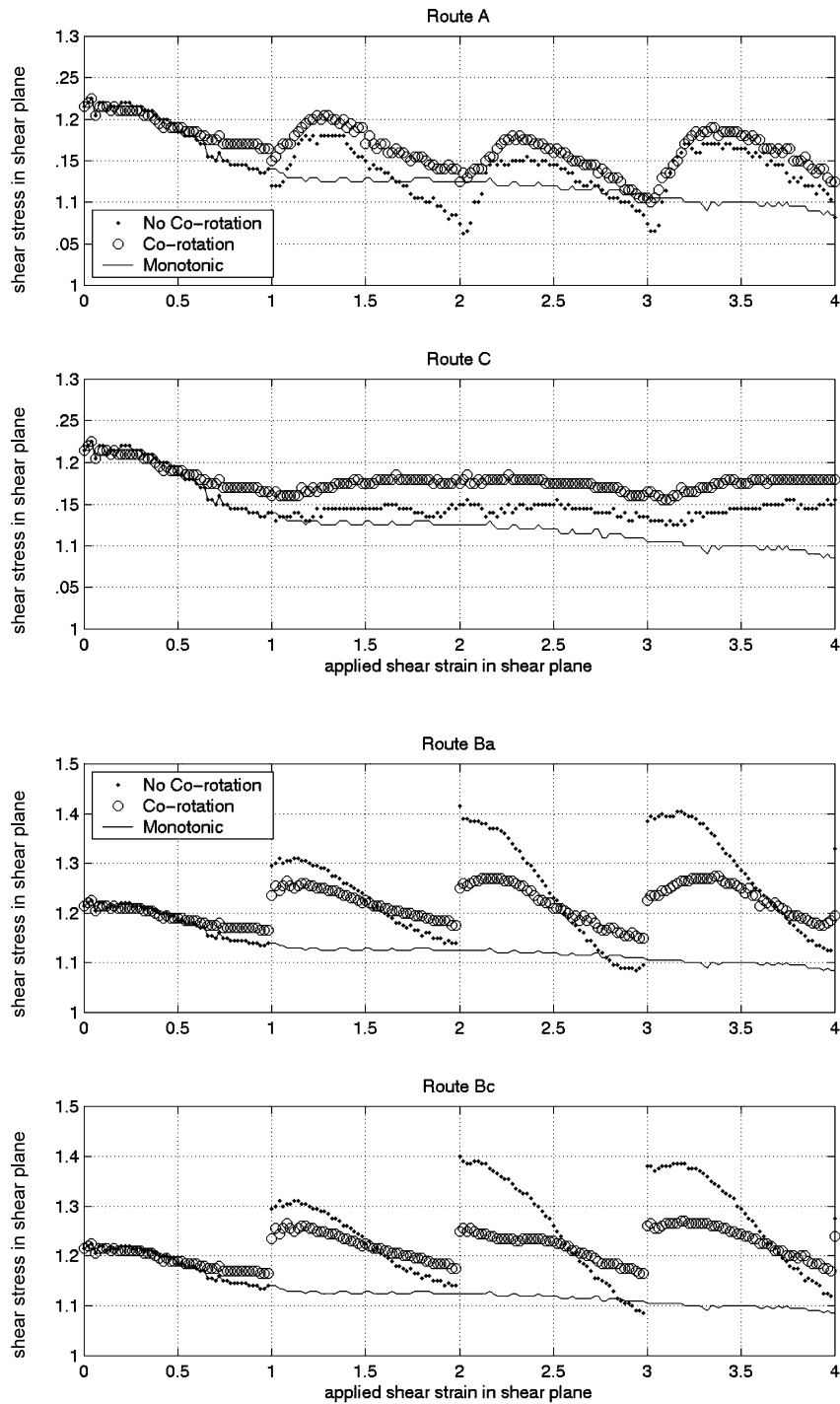


Fig. 4. Evolution of the shear stress–shear strain response along the shear plane of Fig. 1 for A, C, B<sub>A</sub> and B<sub>C</sub>. The die angle is 90° so that a total shear of  $\epsilon_{12} = 1$  is accumulated in each pass (solid dots). We show for comparison the shear stress–shear strain response along the shear plane of Fig. 1 with and without neighboring grain co-rotation. The flow response under monotonic shearing is also shown (thin solid line) to emphasize the influence of strain path changes.

splitting is employed, their shapes become relatively equiaxed with aspect ratios less than the prescribed  $R$ . Differences in their textures will therefore increase with pass number. Interestingly, the shear textures we predict with grain subdivision have features similar to those produced by materials which have developed equiaxed

subgrain microstructures, (see Fig. 1c in [30]). Likewise, the predicted shear textures without splitting are similar to those given by materials which have developed elongated subgrain microstructures, under large shear strains (see Fig. 1k in [30]; the shear plane is horizontal and the shear sense is reversed in [30]).

### 3.2. Flow (shear) stress

Fig. 4a–d displays the evolution of the flow stress with applied shear strain  $\varepsilon_{12}$  along the shear plane ( $\Phi/2$ ) for four passes of each route, A, C, B<sub>A</sub> and B<sub>C</sub>, respectively. The shear strain increases by unity each pass, so the range  $0 < \varepsilon_{12} < 1$  represents the first pass;  $1 < \varepsilon_{12} < 2$ , the second pass and so on. To emphasize the influence of strain path changes, we also superimpose the flow stress evolution under monotonic shear straining with grain subdivision (thin line). Recall that the yield stress predicted by the simulation is only affected by texture evolution. Compared with the initial value of the shear stress, the shear stress at the end of the four passes is not significantly different, but the texture has changed substantially (see Fig. 3). Also by  $\varepsilon_{12} = 4.0$ , the flow stress in the ECAE samples is slightly higher than that of the monotonically sheared sample. The evolution of the shear stress during ECAE deformation is quite revealing of the differences in ECAE routes and resulting deformation textures (also shown in Fig. 4 is the flow stress predicted using the co-rotation scheme, which will be addressed shortly).

In none of the subsequent ECAE passes did the flow response eventually follow the monotonic response. Relative to the monotonic response, we see that changes in strain path can induce hardening–softening due to grain orientations alone (geometric hardening). For the ECAE routes there are two features of interest: (i) the discontinuous change in the yield stress from the end of one pass to the beginning of another, and (ii) the hardening–softening profile associated with each pass.

Transitions in flow stress from pass to pass in Fig. 4 are a direct result of changes between the texture developed in one pass and the shear plane of the next pass. Recall that the grains do not harden. Thus a cross effect or jump in flow stress when transitioning from one pass to another is due to change in strain path and depends on the relative orientation of the texture with respect to the shear plane. In other words, discontinuous changes observed in the yield stress between passes will correspond to discontinuous changes in the overall Taylor factor. The yield stress discontinuity associated with the discontinuity in the Taylor factor is particularly strong for routes B<sub>A</sub> and B<sub>C</sub> (see Fig. 4c and d). In these cases, the material entering each pass is very different than the material exiting the previous pass as Fig. 5 illustrates.

Fig. 5 compares the deformation textures entering and exiting the die for each pass of route B<sub>A</sub>. As shown, pole distributions entering passes 2, 3 and 4 are very different than the characteristic shear texture at the exit of pass 1. Consequently, the sample texture entering the die is initially very resistant to the simple shear deformation of the subsequent pass. Once flow begins, a reorientation of the grains under the simple shear in

passes 2–4 is more favorable, leading to geometric softening.

In routes A and C, the change in orientation of the sample with shear plane translates to a rotation about the 3-axis only, unlike routes B<sub>A</sub> and B<sub>C</sub> [6]. Consequently in routes A and C, we see no discontinuity from pass to pass. For route A, however, some geometric hardening takes place in each pass as the texture evolves to the stable one of the first pass.

The hardening–softening behavior during each pass is dependent on ECAE route. In subsequent passes the textures entering the die are distinct for each ECAE route. With each new strain path, the sample attempts to make a transition from the rotated texture of the previous pass, which is typically several times random (see Fig. 3) to the simple shear texture as developed in the first pass. For example in the cases of cross shear (A, B<sub>A</sub>, and B<sub>C</sub>), this transition to the more favorable orientation forces the grains to reorient along paths which may be geometrically less favorable, leading to substantial initial geometric hardening. This geometric hardening is eventually followed by geometric softening once the grains achieve more favorable orientations to accommodate the imposed shear. Consequently, the evolution of geometric softening reflects the preceding evolution of geometric hardening; that is, within each pass, the more severe the hardening, the stronger the geometric softening that follows. In these cases, the material could soften below the flow stress of the monotonic case (e.g. third pass of routes A and B<sub>A</sub>). Incidentally the strain levels at which geometric hardening–softening occur are not altered by the subdivision criteria employed.

Route C is interesting because unlike the other routes that induce cross shear, the flow stress, and so the texture, is nearly (but not completely) reversed from pass to pass. As seen in Figs. 3 and 4, the texture tends to go from random to shear, from shear back to random, and from random to shear again, and the yield stress shows softening–hardening–softening accordingly. The initial textures and flow stress after shear reversal of the second pass are, however, not quite fully regained. The individual grains have changed orientation and shape under the first pass and hence they do not experience perfect shear strain reversal in the second pass. Incidentally the Baushinger effect, namely, a drop in yield stress upon strain reversal, is linked to internal stresses generated by dislocation accumulation and therefore will not occur in our material with a constant CRSS.

### 3.3. Morphological textures

Within the VPSC model, each grain is treated as an ellipsoidal inclusion characterized by the length and orientation of its principal axes. The evolution of the

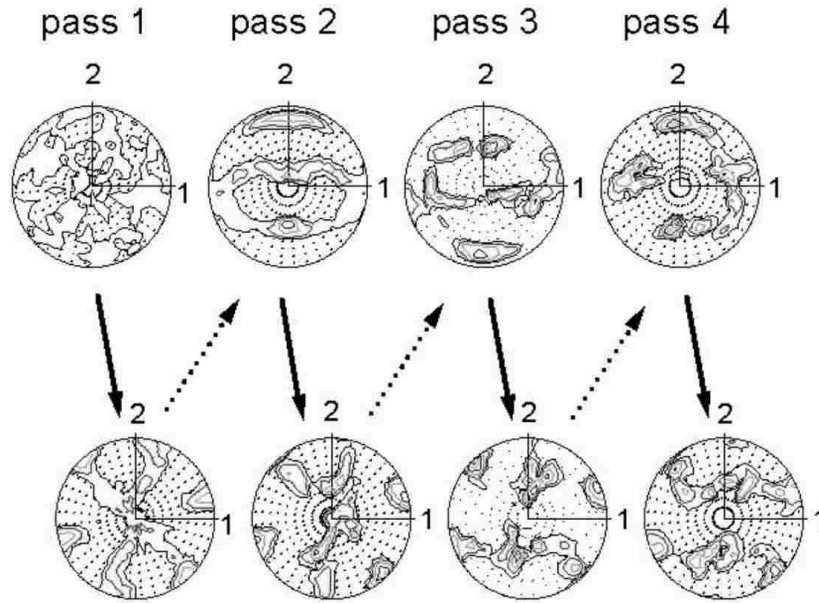


Fig. 5. The top row are the (111) pole figures of the texture in the sample as it enters each pass and the bottom row are the (111) pole figures as the sample exits each pass for route B<sub>A</sub>. Levels 1, 2, 4, 7, 11, 16 multiple of random orientations are plotted.

shape and orientation of each grain is mathematically described by the eigenvalues and eigenvectors of the displacement gradient tensor. As a consequence, we can predict the distribution of the orientation of the long axes of the ellipsoidal grains in the polycrystal, denoted here as the morphological texture. After each pass, the long axis of the grains tends to orient statistically around one direction, which depends on processing route and number of passes. With the exception of samples deformed after shear reversal, there is a slight dispersion ( $\sim +10^\circ$ ) about the maximum density location.

Table 1 shows the angles ( $\Psi$ ,  $\Theta$ ) describing the two sequential rotations needed to reach the location of this maximum after exiting each pass for each route. Fig. 6 illustrates the definition of these angles in the global coordinate system. The first angle  $\Psi$  is measured from the 1-axis when rotated CCW about the global 3-axis. The second angle,  $\Theta$  is measured from the 3-axis when rotated CCW about the new  $2^G$  axis. These angles

correspond to the first two Euler angles associated with the Roe convention.

The evolution of morphological texture was dependent on ECAE route. After the first pass, grains are dispersed between the 0 and  $30^\circ$  around the maximum direction of  $\Psi = 20^\circ$  from the flow axis. After subsequent passes of cross shear, the direction of the long axis tends to rotate towards the flow axis aligning along  $\Psi \sim 15-10^\circ$ . Shear reversal and monotonic straining display the opposite behavior. In the shear reversal route, route C, we find that the grain elongation axis alternates between alignment around  $\Psi = 20^\circ$  after the first and third passes to alignment around  $\Psi = 25^\circ$  after the second and fourth passes. Monotonic shear tends to stabilize the orientation of the long axis at about  $30^\circ$  with increase in strain. For most routes, the long axis of the grains lies within the 1–2 plane (corresponding to  $\Theta \sim 90^\circ$ ) throughout processing. In route B<sub>C</sub>, however,  $\Theta$  decreases with each pass, meaning that the grains

Table 1

The angles ( $\Psi$ ,  $\Theta$ ) describing the position of the maximum intensity in the distribution of the long ellipsoid axis for each pass of the ECAE routes and monotonic case

Route	Pass 1	Pass 2	Pass 3	Pass 4
A	(20°, 90°)	(15°, 90°)	(10°, 90°)	(10°, 90°)
C	(20°, 90°)	(25°, 90°)	(20°, 90°)	(25°, 90°)
B <sub>A</sub>	(20°, 90°)	(15°, 85°)	(15°, 90°)	(15°, 90°)
B <sub>C</sub>	(20°, 90°)	(15°, 85°)	(15°, 81°)	(10°, 76°)
Monotonic	(20°, 90°)	(25°, 90°)	(30°, 90°)	(30°, 90°)

See definition in Fig. 6.

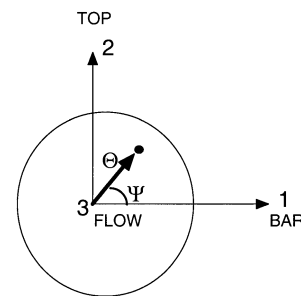


Fig. 6. Schematic defining the angles describing the position of the longitudinal axis of the grains to the global coordinate system. See also Fig. 1.

tend to rotate out of the one to two plane towards the 3-axis with each pass.

Using the geometrically based model of Iwahashi et al. [29], Zhu and Lowe [4] calculate the angle between the grain elongation (longitudinal) axis and the extrusion axis (1-axis), which corresponds to our definition of  $\Psi$  (see Fig. 6), for these four ECAE routes and  $\Phi = 90^\circ$ . Generally our predictions of the distributions of longitudinal grain axis do bound the single value predictions by this model [4,29], with a few exceptions. First, in the third pass of route B<sub>C</sub>, the grain elongation direction is strongly centered around  $\sim 15^\circ$  and not near  $\sim 26.6^\circ$  as predicted by their model. Hence, we predict that the maximum elongation direction of the first pass is not maintained in route B<sub>C</sub>. They [9,29] do predict a steady decrease in the  $\Psi$  angle from 26.6 to 7.1° in four passes for route A and from 26.6 to 10.0° for route B<sub>A</sub>, a trend that is predicted here.

### 3.4. Average grain size and grain subdivision process

We record the evolution of the individual grain shape, number of single and double subdivisions, and the lengths of the average grain shape with applied strain. Fig. 7a shows the evolution of the average length of the long axis for routes A, C, B<sub>A</sub> and B<sub>C</sub> and the monotonic case. The same subdivision criteria Eq. (4) with  $R = 5$  were used for the monotonic case with splitting. For brevity, we display the evolution of the long axis since it experiences the most significant changes. The short axis, for instance, does not change significantly from the end of the first pass to the end of the fourth.

For the ECAE routes, the most significant amount of grain elongation occurs within the first pass, as evident by the initial increase in the long axis  $L$ , followed by a decrease due to grain subdivision. The strain level at which the average  $L$  begins to decrease depends on the value selected for  $R$  in the subdivision criteria Eq. (4). For  $R = 5$ , we find that the largest number of single splits occur in the first pass and the largest number of ‘double splits’, that is disk-like ellipsoidal grains dividing into four smaller equal sized grains, occur in the second pass of the cross-shear routes. However, not all grain orientations subdivided in the first pass; without subdivision, the average aspect ratio after the first pass is  $\sim 6.0$ .

Fig. 7b shows progression of the accumulated number of long axis divisions for routes A, C, B<sub>A</sub> and B<sub>C</sub> and the monotonic case, as the long axis subdivisions occur more often than the medium axis subdivisions for  $R = 5$ . As shown, the subdivision process highly depends on ECAE route. In subsequent passes 2 through 4 of cross shear, this process of grain deformation and subdivision generally continues and the grains further refine with each pass. In route C, however, the grain long axis

shortens in the second pass and elongates in the third pass, without grain subdivision.

Comparing the accumulated number of splits with the evolution of average grain size in Fig. 7, reveals that there are two reasons for a decrease in the length of the long and medium axes: deformation and grain subdivisions. The reduction by deformation is evident during those deformation steps that result in a decrease in these grain axes with no concomitant subdivision activity (a plateau in Fig. 7b). The second one is evident when we observe a relatively abrupt decrease in grain size associated with much splitting activity (non-zero, positive slope in Fig. 7b). For instance in monotonic straining and route A, grain size reduction clearly occurred by grain splitting. The number of subdivisions in monotonic straining was the highest, followed by route A, and generally increased with strain in these cases. However, for route C, the grain size reduced in the second and fourth passes due to deformation by reverse shear. In the beginning of the third and fourth passes of B<sub>C</sub>, the length of the long axes decreased due to deformation by redundant strain since there were no associated long axes subdivisions.

These predictions show that the ECAE processing route had a significant influence on grain refinement. In Table 2, we report the average grain axes lengths, and their coefficient of variation (COV), or ratio of the standard deviation to the mean, after  $N = 4$  passes for each route and the monotonic case. All grain axis lengths are initially unity. Based on our subdivision rule, we also estimate the relative reduction in grain volume (proportional to the product of all grain axes) or the ratio of the final–initial grain volume  $V_R$ , after  $N$  passes<sup>6</sup> as:

$$V_R(N) = \left(\frac{1}{2}\right)^m \quad \text{where } m = (x_L(N) + x_M(N)) \quad (5)$$

In Eq. (5),  $x_L(N)$  is the total number of long axis splits and  $x_M(N)$  is the total number of medium axis subdivisions per grain after  $N$  passes. Monotonic applied shear strain resulted in the most grain refinement, representing a reduction by an order of magnitude lower than that by routes B<sub>A</sub> and B<sub>C</sub>, yet with approximately the same aspect ratio. Apart from the monotonic case, route A gave the most refinement, followed by routes B<sub>A</sub>, then B<sub>C</sub>, and finally C with the least amount of grain refinement. As listed, routes B<sub>C</sub> and B<sub>A</sub> produced the most dispersion in grain size and route C the least. In these extreme cases, the small axis ranged from 0.08 to

<sup>6</sup> Eq. (5) is a more representative calculation of the volume reduction than the product of the average lengths of the ellipsoid after four passes listed in Table 2, though the two estimates give similar values.

0.8 for route B<sub>C</sub> and the long axis ranged from 0.82 to 1.36 for route C, respectively.

The last column of Table 2 reports the long to short axis aspect ratio for the routes as an indication of their effectiveness in producing an equiaxed microstructure. Route A produced mostly elongated grains, even after four passes, as seen experimentally [1]. Route B<sub>C</sub> produced more equiaxed grains than routes B<sub>A</sub> or A, which is in agreement with [6,7]. Route C appears to be

the most effective in producing equiaxed grains, which has been observed experimentally [1,5]. However, in route C, the grains contract on even passes, and therefore, the apparent equiaxed grain structure after the fourth pass is a result of the initial spherical grain shape [1]. We suspect that results for route C, unlike the other routes, will be more sensitive to whichever mechanism of subgrain formation that we implement in future simulations. The present simulation allowed the grains to easily

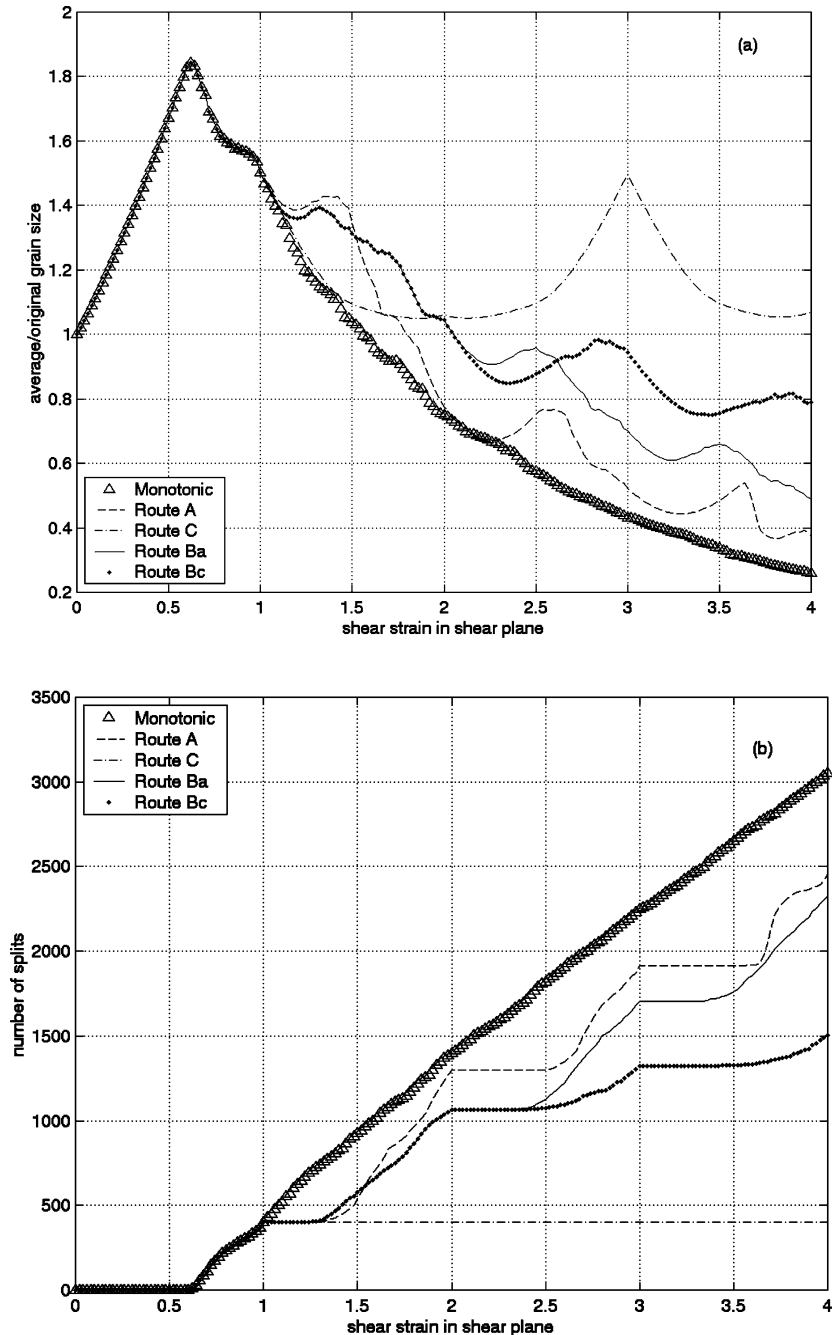


Fig. 7. (a) Evolution of average length of the long grain axis, and (b) number of long axis subdivisions accumulated with applied shear strain for all four ECAE routes and monotonic shear straining.

Table 2

Ratios of the final to initial average values of each axis of the grain and the COV (in parentheses) after four passes

Route (4 passes)	Long axis (COV)	Medium axis (COV)	Short axis (COV)	Final volume	Aspect ratio $L/S$
A	0.37 (0.24)	0.24 (0.21)	0.09 (0.22)	$7.67 \times 10^{-3}$	4.1
C	1.07 (0.08)	0.92 (0.14)	0.59 (0.36)	$5.42 \times 10^{-1}$	1.8
B <sub>A</sub>	0.49 (0.41)	0.26 (0.31)	0.14 (0.29)	$1.48 \times 10^{-2}$	3.5
B <sub>C</sub>	0.79 (0.33)	0.40 (0.40)	0.25 (0.36)	$6.65 \times 10^{-2}$	3.2
Monotonic	0.26 (0.23)	0.15 (0.10)	0.07 (0.008)	$2.06 \times 10^{-3}$	3.7

The subdivision rule assumes that when either criterion (4) is satisfied (for  $R = 5$ ), the grain subdivides in half. Initially all grain axis lengths are equal. The ‘final volume’ reported is the ratio of the final to initial volume and is calculated using Eq. (5). The monotonic case corresponds to simple shear without sample rotation up to  $\varepsilon_{12} = 4.0$ .

lengthen in one pass and shorten in the next in route C, a process that may be impeded by the formation of cells in the grain.

### 3.5. Grain size distributions

Table 2 reports estimates that provide only some information of the microstructure. It has been observed that the dispersion in the grain size in ECAE materials is broad and in some cases, follows a log-normal distribution [31]. Similarly we find that the  $L$ ,  $M$ , and  $S$  lengths had significant statistical variation, which strongly depends on processing route. We fit four samples, one of each of the three axes and a fourth sample including all axes, to several types of statistical distributions, namely Gaussian (normal), log normal, Weibull, and double exponential. Many physical distributions in nature fit one of these four statistical distributions. In all cases, the grain size samples were neither Gaussian, double exponential, nor Weibull. In some cases, they were clearly log-normal.

Let  $P(X < x)$  be the probability that the actual grain axis length  $X$  is at most  $x$ . The two parameter log-normal ( $\mu$ ,  $\sigma$ ) cumulative distribution function for  $P(X < x)$  is

$$P(X \leq x) = \int_{-\infty}^{\ln x} \frac{1}{\sqrt{2\pi}\sigma} \exp\left[-\frac{(t - \mu)^2}{2\sigma^2}\right] dt, \quad 0 \leq x < 8 \quad (6)$$

where  $\mu$  and  $\sigma$  are the two log-normal parameters defining location and dispersion, respectively. The mean and variation in  $X$  are related to ( $\mu$ ,  $\sigma$ ) according to

$$\text{Mean} = \exp\left[\mu + \frac{\sigma^2}{2}\right]$$

$$\text{Variance} = \exp[2\mu + \sigma^2](\exp[\sigma^2] - 1) \quad (7)$$

Fig. 8 shows these statistical distributions for routes B<sub>A</sub> and B<sub>C</sub>, after the fourth pass on ‘log-normal probability paper’, wherein the axes of a  $P(X < x)$  versus  $x$  plot are scaled such that a log-normal distribution would plot as a straight line. As shown, for routes B<sub>A</sub> and B<sub>C</sub>, we find that the distribution of the long, medium and short axis

lengths follow very well a log-normal distribution, after four passes. When sampling all grain axes, as would be obtained in a 2-D cross-sectional image, there is, of course, much more variation. The log-normal parameters ( $\mu$ ,  $\sigma$ ) are summarized in Table 3.

Microstructures associated with routes A and C, on the other hand, were bi-modal and hence did not follow one of the four distributions tested. They had a wide dispersion of grain sizes, consisting of many relatively large and small grains. In route A, we find that there are many smaller size grains with some elongated grains. In route C, the opposite is true; route C produced a large population of elongated grains and a smaller fraction of small grains.

### 3.6. Influence of grain shape and grain co-rotation

All the model calculations reported in this paper account for the evolution of the shape of each grain and subdivision based on individual grain shapes, leading to the predicted dispersion in grain shapes seen in Fig. 8. Our criteria also limit the aspect ratio of the grain to  $R$ . It is therefore reasonable to ask to what extent do our grain refinement criteria and/or the dispersion in grain shape affect the macroscopic response. Differences in flow stress with and without grain subdivision become noticeable by the second pass of route C and the 3rd pass of the other routes. To analyze the influence of dispersion in grain shape, these results were compared with those obtained by assuming each grain had the same shape, which was updated in each step in the simulation, a substantially faster calculation. We find that differences in the flow stress and texture evolution between the two calculations become pronounced by the fourth pass of each route.

Enforcing neighboring grain co-rotation influenced the evolution of flow stress and texture by the end of the first pass. Textures are more disperse, evolve slower and achieve lower maximum intensities when using the co-rotation scheme [27] yielding better agreement with texture measurements [28]. Textures are qualitatively similar to the ones obtained without co-rotation (see Fig. 3) and are not shown here. As a consequence, the

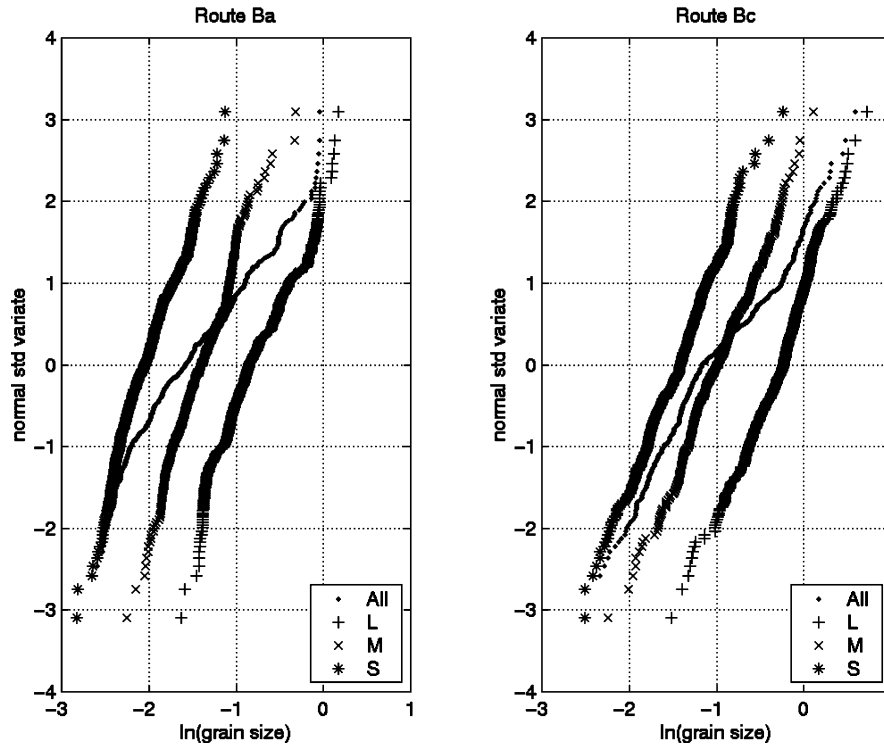


Fig. 8. Lognormal plots of the distribution of grain sizes for ECAE (a) route B<sub>A</sub> and (b) route B<sub>C</sub> after four passes.

stress–strain curves predicted with the co-rotation scheme display substantially less geometric hardening for the four routes, as shown in Fig. 4. This neighbor co-rotation only influenced significantly the grain size distribution of route A, resulting in a slightly smaller average grain size ( $L=0.34$ ) and higher variation ( $\text{COV}=0.33$ ). The grains elongated and split in each pass more so in route A than in the other routes, and hence the dispersive effects of grain–grain interactions are more pronounced in route A.

#### 4. Discussion

In this initial work of model development, we assume a constant CRSS for the single crystal in our FCC polycrystal in efforts to isolate the influence of shear plane and texture orientations. Secondly we employ a subdivision criteria based only on a critical grain shape, which modifies shape and size, but not orientation. In reality, grain subdivision is a far more complicated

stochastic process than the shape-based idealization employed here. For direct comparison with data, our single crystal constitutive law should account for the coupling between grain refinement and hardening due to intragranular microstructures. Nonetheless, in this section we make some qualitative comparison with experimentally observed and measured trends, and discuss the consequences of these two modeling assumptions in the context of such comparisons.

##### 4.1. Qualitative comparison with current experimental data

Using our ‘shape-based’ criteria, monotonic straining had the largest number of splits per strain increment compared with the ECAE routes (see Fig. 6a) and route A had the largest among the ECAE routes. Using this scheme rapid grain refinement of route A is not surprising. The deformation path or sequences of rotations provided by route A continually distorted the sample in the 1–2 plane [6] and caused the grains to

Table 3

Estimates for location  $\mu$  and variance  $\sigma$  parameters associated with the log normal distribution Eq. (6) for samples of the long, medium, short and all grain axes after four passes of routes B<sub>A</sub> and B<sub>C</sub>. They are related to the sample mean and variance of the grain size by Eq. (7).

Route	$\mu$ (L)	$\sigma$ (L)	$\mu$ (M)	$\sigma$ (M)	$\mu$ (S)	$\sigma$ (S)	$\mu$ (All)	$\sigma$ (All)
B <sub>A</sub>	−0.79	0.39	−1.40	0.31	−2.04	0.31	−1.54	0.62
B <sub>C</sub>	−0.29	0.32	−0.98	0.37	−1.45	0.35	−1.01	0.60

continually elongate, favoring grain refinement by our criteria. Observations by [1] on Ni support this result. As shown in Fig. 4, route A provides more continuity in material mechanical response (i.e. yield stress) between passes than routes  $B_C$  or  $B_A$ , yet it is not a continuous deformation process. Also we show that the deformation textures of route A after four passes have very similar features to the simple shear texture monotonically strained up to  $\epsilon_{12} = 4.0$ , as well as average grain aspect ratio and final volume (see Table 2).

Route C had the least number of splits and splits/deformation. Since it is experimentally proven that significant grain refinement takes place for route C, the latter result suggests that it will occur primarily by subgrain formation, with little to no contribution from shape effects. Indeed in a related study [32], substantial grain refinement of pure Al after four cycles was observed as a result of shear band formation within elongated grains. In their die system [32], the amount of deformation accumulated per forward–reverse cycle was 0.9, less than half of that accumulated in two passes of route C with  $\Phi = 90^\circ$ . After further cycling, 20–100 cycles, an equiaxed subgrain structure was formed as a result of intersecting shear bands; this latter fragmentation process was found to proceed at a much slower rate than the initial formation of shear bands after 24 cycles [32].

Interestingly with respect to reducing the grain size, the predicted trends qualitatively agree best with the redundant strain theory proposed by Prangnell et al. [9] and for the most part, with the trends seen in their FCC Al–Mg alloy ECAE studies, though they used  $\Phi = 120^\circ$  and  $N = 16$ . Like our model predictions they found that  $B_A$  and  $B_C$  led to less grain refinement than route A, and route C was the least effective. In our model, grain refinement was affected by this redundant strain; that is, when the shear strain experienced by the sample is reversed, as in the even passes of route C or the third pass of route  $B_C$ , most of the grains tend to deform to a lower aspect ratio and therefore they are less likely to meet the split criteria and refine. Grain length contraction by deformation would hinder grain subdivision in the case of route  $B_C$ , which is why route  $B_A$  is predicted to be more effective than  $B_C$ .

Model predictions and data, however, do not quantitatively agree. Within the first four passes, the model predicts that the grain volume on average refines by one to two orders of magnitude compared with up to nine orders of magnitude (depending on the initial grain size) typically observed experimentally after one to four passes [7,33]. The latter statistics typically include subgrains, whereas our subdivision criteria currently do not discriminate between low and high angle boundary misorientations and hence newly subdivided grains are simply smaller grains. Nonetheless, we could have altered our empirical subdivision criteria to in-

crease the number of subdivisions each time the criteria are satisfied, and/or use, for instance, a lower value of 2 for  $R$  (though in one study for routes A and C [33], the aspect ratios do remain below 5). However, this would be a highly empirical approach and, instead, we propose to direct our future ECAE model modifications towards incorporating more realistic subgrain structure formation and evolution.

With respect to generating an equiaxed structure we predict that C and  $B_C$  are more effective than  $B_A$  and A after four passes. The equiaxed structure of these two routes results from the partial recovery of the initial spherical grain shape during passes of redundant strain. Microstructure formed under route C is more sensitive to pass number since shear reversal is sequential. After even (reverse shear) passes, route C produces equiaxed grains, yet after odd (forward shear) passes, the elongated grain shapes of the first pass are restored. Experimental studies [1,9] on Ni and Al processed by route C observe these same microstructural changes. The shear reversal in route  $B_C$ , however, is not sequential. We predict that the morphological and crystallographic textures developed in route  $B_C$  are altered sufficiently between the second and third pass such that deforming back to the initial random microstructure is difficult. Many studies observe that  $B_C$  is the most effective for creating an equiaxed, submicron grain structure.

#### 4.2. Grain refinement effectiveness: experimental evidence

Most experimental studies for pure Al using an ECAE  $\Phi = 90^\circ$  die [6,8], find that route  $B_C$  is more effective than route A and C in producing both an equiaxed, refined microstructure. Nonetheless, there are other studies that observe the contrary [4,5,9], a fact that is not at all surprising when one considers the several factors that can influence microstructural evolution during ECAE.

- 1) The final grain size will depend on material, processing temperature, processing rate, and alloying element [3].
- 2) The ECAE deformation grain structures are very unique, inhomogeneous, and it can be difficult to characterize the grain size, and distinguish between grains, subgrains, cell blocks and deformation bands [2]. Particularly when the distribution is very inhomogeneous, average values of grain size can be biased since most of the larger grains will be missed in the sampling. As Prangnell et al. [9] point out, these larger ones usually do not get counted in the statistics since they are bigger than the sampling area.

- 3) An ECAE route's effectiveness in grain refinement has been defined by several characteristics. With respect to creating a more equiaxed homogeneous grain structure, Ferrasse et al. [5] find that route C is more successful than route B<sub>C</sub> or A for Cu and Al alloys. However, based on a review of results for  $\Phi = 90^\circ$  to date, Oh-Ishi et al. [8] conclude that B<sub>C</sub> is the most effective, then C and lastly A and B<sub>A</sub> are the least effective in producing a homogeneous, refined microstructure. Grain refinement can also be based on the fraction of high angle grain boundaries. Typically the subgrains become grains when they have high angle grain boundaries. When this distinction between grains and subgrains is made, routes A, B<sub>A</sub> and C are less efficient at eliminating subgrain structures than route B<sub>C</sub> after four or more passes [6–8]. Consequently route B<sub>C</sub> will be considered more effective than routes A and C, even if route B<sub>C</sub> produces subgrain structures that are slightly larger [7], and more effective than B<sub>A</sub> even if B<sub>C</sub> and B<sub>A</sub> produce the same size subgrains [8,9].
- 4) Grain refinement effectiveness is also highly dependent on die angle [6,7,9,10,34]. Route A seems to be the most effective in grain refinement for  $\Phi = 120^\circ$  [9], whereas B<sub>C</sub> is the most effective for  $\Phi = 90^\circ$  [6,7]. Chakkingal et al. [34] found that the subgrains were misoriented only  $\sim 1\text{--}4^\circ$  and the deformation textures were not strong after 6 passes using three processing routes and  $\Phi = 135^\circ$ . On the contrary, studies using  $\Phi = 90^\circ$  find that the deformation textures are extremely strong [14].
- 5) The initial textures and grain shapes of material used from study to study may be different. For instance, for route C, in which the initial texture is partially recovered in the even passes (see Fig. 3), the influence of initial texture on the final texture could be strong and depend on pass number. Particularly in routes B<sub>C</sub> and C, there may be a relation between the initial grain shape and the final grain shape distribution that is partially recovered in these routes which have redundant strain.

Based on a comprehensive study of experimental work, Zhu and Lowe [4] present a hypothesis on the mechanism of grain refinement. They propose that effective grain refinement happens when the angle between the texture plane (defined as the plane whose normal coincides with the maximum intensity of the (111) pole figure) and the shear plane coincides with the angle between two slip planes in a crystal ( $70.53^\circ$  for a FCC crystal). For each pass of each route we list in Table 4 the angle  $\Omega$  between the (111) maximum density pole and the shear plane normal (axis 2' in Fig. 1a) as measured clockwise from the 2' axis when rotated about the 3-axis. According to our predictions, none of the

Table 4  
Estimates for the angle  $\Omega$  between the shear plane normal and the (111) maximum density pole of the sample as it enters passes 2–4

Route	Entering pass 2	Entering pass 3	Entering pass 4
A	40°	90°	90°
B <sub>A</sub>	45°	50°	50°
B <sub>C</sub>	45°	40°	41°
C	60°	0°	65°

routes satisfies this criterion exactly. Considering the texture/shear plane orientation of  $\Omega$  alone, routes B<sub>A</sub> and B<sub>C</sub> may best facilitate shear deformation by slip via a reduction of the Schmid factor since their maximum density pole location is close to  $\Omega = \sim 45^\circ$  from the shear plane. This certainly aids in the significant geometric softening seen in Fig. 4 during each pass in these routes.

This brief comparison suggests that studying the maximum density pole or  $\Omega$  may not be the determining factor. One advantage of predicting the orientation distributions or plotting pole figures, such as in Figs. 3 and 5, is that they display the distribution of (111) poles, perhaps with many local maxima, whereas the maximum density pole on which the hypothesis is based is a single point. Furthermore, consideration of grain–grain interactions and misorientations within the grains will only spread the grain crystallographic (and morphological) orientations further. Lastly  $\Omega$  will change throughout ECAE straining.

## 5. Conclusions

In this work, a VPSC constitutive model was used to perform a systematic study of texture development associated with different ECAE histories, for  $\Phi = 90^\circ$  and a single phase FCC polycrystalline material. We elected to study FCC in the present work in order to ease interpreting the relationship between texture development and ECAE processing route. We also assumed a constant CRSS for the single crystal, which allowed us to uncouple geometric hardening from dislocation hardening effects. Capturing the latter effect is more difficult, since dislocation hardening at large strain needs to account for the evolution of cells and subgrain microstructure. Lastly an empirical grain subdivision model was employed to represent microstructural evolution.

After only four passes, several distinctions between the four standard processing routes, A, B<sub>A</sub>, B<sub>C</sub> and C, can already be made. The most important conclusions from this work are (i) comparisons with monotonic shear strain deformation reveal that the strain path changes introduced by these ECAE routes have a significant impact on the macroscopic flow response,

grain shape and size distribution, and morphological and crystallographic textures. (ii) The morphological and crystalline textures developed are quite strong. The evolution of crystallographic texture is highly dependent on processing route, leading to non-negligible geometric hardening and softening, reflecting the orientation changes of the polycrystal associated with strain path changes. Hence the directional properties of ECAE materials will depend on processing route. (iii) Neighboring grain–grain interactions cannot be neglected and tend to weaken texture evolution in all routes. (iv) Modeling dispersion in grain shape and size and grain subdivision altered texture evolution by the end of the third pass, i.e.  $\epsilon_{12} > 2.0$ . (v) When allowing the severely deformed grains to continually divide into half, the model predicts that monotonic shear straining was the most effective, followed by route A, B<sub>A</sub>, B<sub>C</sub> and C in descending order of grain refinement effectiveness after four passes. However, for producing refined equiaxed grains, route B<sub>C</sub> was more effective than routes B<sub>A</sub> and A.

An aspect of ECAE that is crucial to capture correctly is the grain refinement process. Here we use simple criteria for grain subdivision, which are satisfied when the ratio of the grain main axes reaches an empirical threshold value. Clearly, the subdivision process is more complicated than modeled here by simple morphological considerations, and a more physically motivated criterion needs to be implemented for rigorous comparisons with experiments.

Finally, a proper simulation of the ECAE process should account for the geometry of the die, friction effects, heterogeneous deformation and specific boundary conditions. For performing such simulations we envision interfacing the VPSC polycrystal model with a finite element code which would account for these processing aspects of the problem. The feasibility of such approach has been recently demonstrated by us for the particular case of inhomogeneous deformation of Zr [20].

## Acknowledgements

This work was supported by the Division of Materials Science of the Office of Basic Energy Sciences of the US DOE.

## References

- [1] V.M. Segal, Mater. Sci. Eng. A197 (1995) 157–164.
- [2] R.Z. Valiev, I.V. Alexandrov, Y.T. Zhu, T.C. Lowe, J. Mater. Res. 17 (2002) 5–8.
- [3] S.L. Semiatin, P.B. Berbon, T.G. Langdon, Scr. Mater. 44 (2001) 135–140.
- [4] Y.T. Zhu, T.C. Lowe, Mater. Sci. Eng. A291 (2000) 46.
- [5] S.V. Ferrasse, M. Segal, K.T. Hartwig, R.E. Goforth, Metall. Mater. Trans. A 28 (1997) 1047.
- [6] M. Furukawa, Y. Iwahashi, Z. Horita, M. Nemoto, T.G. Langdon, Mater. Sci. Eng. A257 (1998) 328.
- [7] Y. Iwahashi, Z. Horita, M. Nemoto, T.G. Langdon, Acta Mater. 46 (1998) 3317.
- [8] K. Oh-Ishi, Z. Horita, M. Furukawa, M. Nemoto, T.G. Langdon, Metall. Mater. Trans. A 29 (1998) 2011.
- [9] P.B. Prangnell, A. Gholinia, M.V. Markushev, in: T.C. Lowe, R.Z. Valiev (Eds.), Investigations and Applications of Severe Plastic Deformation, Kluwer Academic Publishers, The Netherlands, 2000, p. 65.
- [10] K. Nakashima, Z. Horita, M. Nemoto, T.G. Langdon, Acta Mater. 46 (1998) 1589–1599.
- [11] B. Peeters, M. Seefeldt, C. Teodosiu, S.R. Kalidindi, P. Van Houtte, E. Aernoudt, Acta Mater. 49 (2001) 1607.
- [12] R.A. Lebensohn, C.N. Tomé, Acta Metall. Mater. 41 (1993) 2611.
- [13] U.F. Kocks, C.N. Tomé, H.-R. Wenk, Texture and Anisotropy, second ed., Cambridge University Press, Cambridge, 2000.
- [14] S.R. Agnew, U.F. Kocks, K.T. Hartwig, J.R. Weertman, Proceedings of the 19th Risø International Symposium on Materials Science, Risø National Laboratory, Roskilde, Denmark, 1998, p. 201.
- [15] P.S. Follansbee, U.F. Kocks, Acta Metall. 36 (1988) 81.
- [16] S. Kok, A.J. Beaudoin, D.A. Tortorelli, Acta Mater. 50 (2002) 1653–1667.
- [17] A.J. Beaudoin, A. Acharya, S.R. Chen, D.A. Korzekwa, M.G. Stout, Acta Mater. 48 (2000) 3409.
- [18] H. Gao, Y. Huang, W.D. Nix, J.W. Hutchinson, J. Mech. Phys. Solids 47 (1999) 1239.
- [19] Y. Iwahashi, J. Wang, Z. Horita, M. Nemoto, Scr. Mater. 35 (1996) 143.
- [20] C.N. Tomé, P.J. Maudlin, R.A. Lebensohn, G.C. Kaschner, Acta Mater. 49 (2001) 3085.
- [21] R.W. Cahn, P. Haasen, E.J. Kramer (Eds.), Plastic Deformation and Fracture of Materials. Materials Science and Technology: A Comprehensive Treatment, vol. 6, VCH, New York, 1993.
- [22] D.A. Hughes, N. Hansen, Acta Mater. 45 (9) (1997) 3871.
- [23] X. Huang, Scr. Mater. 38 (11) (1988) 1697.
- [24] P.L. Sun, P.W. Kao, C.P. Chang, Mater. Sci. Eng. A283 (2000) 82.
- [25] I.J. Beyerlein, R.A. Lebensohn, C.N. Tomé, in: Y.T. Zhu, T.G. Langdon, R.S. Mishra, S.L. Semiatin, M.J. Saran, T.C. Lowe (Eds.), Ultrafine Grained Materials II. The Minerals, Metals and Materials Society, 2002, p. 585.
- [26] R.A. Lebensohn, Acta Mater. 49 (2001) 2723.
- [27] C.N. Tomé, R.A. Lebensohn, C.T. Necker, Metall. Mater. Trans. A (2002), in press.
- [28] S. Vogel, I.J. Beyerlein, M.A.M. Bourke, D.W. Brown, C.N. Tomé, T.G. Langdon, Cheng Xu, Mater. Sci. Forum 408–412 (2002) 673–678.
- [29] Y. Iwahashi, M. Furukawa, Z. Horita, M. Nemoto, T.G. Langdon, Metall. Mater. Trans. 29A (1998) 2245.
- [30] D.A. Hughes, R.A. Lebensohn, H.R. Wenk, A. Kumar, Proc. R. Soc. London A 456 (2000) 921.
- [31] T. Ungar, I.V. Alexandrov, P. Hanak, in: T.C. Lowe, R.Z. Valiev (Eds.), Investigations and Applications of Severe Plastic Deformation, Kluwer Academic Publishers, The Netherlands, 2000, p. 133.
- [32] A. Korbel, M. Richert, J. Richert, Proceedings of the Second Risø International Symposium on Metallurgy and Materials Science, Risø National Laboratory, Roskilde, Denmark, 1981, p. 445.
- [33] Y. Iwahashi, Z. Horita, M. Nemoto, T.G. Langdon, Acta Mater. 45 (1997) 4733–4741.
- [34] U. Chakkingal, A. Suriadi, P.F. Thomson, Mater. Sci. Eng. A266 (1999) 241.